

Optimization with nonstationary, nonlinear monolithic fluid-structure interaction

Thomas Wick¹ and Winnifried Wollner²

¹Leibniz Universität Hannover, Institut für Angewandte Mathematik, AG Wissenschaftliches Rechnen, Welfengarten 1, 30167 Hannover, Germany

²Technische Universität Darmstadt, Fachbereich Mathematik, Dolivostrasse 15, 64293 Darmstadt, Germany

Abstract

Within this work, we consider optimization settings for nonlinear, nonstationary fluid-structure interaction. The problem is formulated in a monolithic fashion using the arbitrary Lagrangian-Eulerian framework to set-up the fluid-structure forward problem. In the optimization approach, either optimal control or parameter estimation problems are treated. In the latter, the stiffness of the solid is estimated from given reference values. In the numerical solution, the optimization problem is solved with a gradient-based solution algorithm. The nonlinear subproblems of the FSI forward problem are solved with a Newton method including line search. Specifically, we will formally provide the backward-in-time running adjoint state used for gradient computations. Our algorithmic developments are demonstrated with some numerical examples as for instance extensions of the well-known fluid-structure benchmark settings and a flapping membrane test in a channel flow with elastic walls.

1 Introduction

This paper is devoted to the study of optimal control and parameter estimation problems of nonstationary, nonlinear fluid-structure interaction (FSI). For general overviews on the FSI forward problem, we refer to the books [10, 26, 29, 9, 4, 7, 52, 28]. Fluid-structure interaction is still one of the most challenging problem settings within multiphysics applications. The main reason being that the dynamics of both subproblems are exchanged on the interface and accurate discretizations are therefore necessary. Secondly, numerical algorithms are sensitive in terms of stability to the physical parameters; known as added-mass effect [11, 27, 2, 56]. As coupling strategy we choose, in this work, the well-known arbitrary Lagrangian-Eulerian (ALE) technique [17, 42, 25].

Employing FSI as forward problem within an optimization framework contains the previously mentioned difficulties and yields significant further challenges when dealing with nonstationary problem settings. Historically, this subject falls into the category of PDE-constrained optimization [46]. Studies concentrating on theoretical and computational aspects for stationary FSI optimization are

[53, 57, 60, 12]. Here, we notice that the required adjoints are the same as used for adjoint-based error estimation; see for instance [62, 51]. Nonlinear (stationary) FSI investigating various partitioned coupling techniques was recently subject in [54]. The by far more challenging situation of nonstationary settings is listed in the following. A nonstationary situation assuming a rigid solid was theoretically studied in [48]. Further theoretical results for a boundary control FSI problem were established in [8]. Parameter estimation to detect the stiffness of an arterial wall with a well-posedness analysis and numerical simulations was addressed in [49]. Again in blood flow simulations, a data assimilation problem was formulated in [33], in which however, the arterial walls were not considered. A full FSI problem for data assimilation using a Kalman filter was subject in [6]. In [44], the authors used optimization techniques to formulate the FSI coupling conditions. Adjoints for 1D FSI were derived in [16, 47]. Reduced basis methods for FSI-based optimization were developed in [45]. Optimal control of nonstationary FSI applied to benchmark settings was investigated in [3]. A linearized FSI optimization problem was addressed in [23] and detailed results for full-time-dependent FSI optimal control were summarized in [22]. In this respect, we also mention [24] in which the adjoints required for optimization were employed for dual-weighted residual error estimation for time adaptivity. Most recently, a uncertainty quantification framework for fluid-structure interaction with applications in aortic biomechanics was developed in [43].

The significance of the current work is on the development of a robust fully monolithic formulation for gradient-based optimization for nonstationary, nonlinear FSI problems. Here, the coupled problem is prescribed in the reference configuration with the help of the ALE approach in a variational-monolithic way. As previously summarized in our literature review, only very few results exist to date for such a framework. Indeed the challenges consist of both the nonlinearities and the nonstationary nature of the problem. FSI in the forward state is itself a highly nonlinear problem. Moreover, interesting nonstationary configurations require several thousands of time steps. For instance the FSI 3 benchmark [41, 9] requires about 6 000 to 10 000 time steps for a fully developed oscillatory solution. These are costly computations, even for a moderate number of spatial degrees of freedom. Numerically, an inf-sup stable spatial discretization is applied to the FSI forward problem. Time discretization is based on a one-step-theta formulation. The discretized subproblems are solved with Newton solver including line search. In order to apply gradient-based techniques, the adjoint state is running backwards in time and must access the primal solution at the time points when treating nonlinear problems. Such derivations and implementations are very tedious. In this work, we carefully derive and implement them in order to test their performance. These are tested with the help of the modification of well-known FSI benchmark settings [41, 9] and a flapping membranes example that was originally proposed in [30] and later modified in [59].

The outline of this paper is as follows: In Section 2, the equations for fluid flow and solids are summarized. Moreover, the FSI setting is formulated in a monolithic fashion using the arbitrary Lagrangian-Eulerian framework. Section 3 contains temporal and spatial discretizations. The main results are presented in Section 4 in which the gradient computation, including details on the adjoint, are presented. In Section 5 the solution algorithms for the FSI optimization framework are presented.

Our algorithmic techniques are substantiated with several numerical tests in Section 6. We summarize our main findings in Section 7.

2 Modeling the FSI forward problem

2.1 Notation

We denote by $\Omega := \Omega(t) \subset \mathbb{R}^d$, $d = 2$, the domain of the FSI problem. The domain consists of two time-dependent subdomains $\Omega_f(t)$ and $\Omega_s(t)$. The FSI-interface between $\Omega_f(t)$ and $\Omega_s(t)$ is denoted by $\Gamma_i(t) = \overline{\Omega_f(t)} \cap \overline{\Omega_s(t)}$. The initial (or later reference) domains are denoted by $\widehat{\Omega}$, $\widehat{\Omega}_f$ and $\widehat{\Omega}_s$, respectively, with the interface $\widehat{\Gamma}_i = \overline{\widehat{\Omega}_f} \cap \overline{\widehat{\Omega}_s}$. Furthermore, we denote the outer boundary by $\partial\widehat{\Omega} = \widehat{\Gamma} = \widehat{\Gamma}_{\text{in}} \cup \widehat{\Gamma}_D \cup \widehat{\Gamma}_{\text{out}}$ where $\widehat{\Gamma}_D$ and $\widehat{\Gamma}_{\text{in}}$ are Dirichlet boundaries (for the velocities and displacements) and $\widehat{\Gamma}_{\text{out}}$ denotes a fluid outflow Neumann boundary, respectively. The displacements are set to zero on $\widehat{\Gamma}_{\text{out}}$.

As frequently used in the literature, we denote the L^2 scalar product in Ω with $(a, b) := (a, b)_\Omega := \int_\Omega a \cdot b \, dx$ for vectors a, b . For (2nd order) tensor-valued functions A, B , it yields $(A, B) := (A, B)_\Omega := \int_\Omega A : B \, dx$, where $A : B = \sum_{ij=1}^d A_{ij} B_{ij}$ and A_{ij} and B_{ij} are the entries of A and B .

2.2 Spaces

For the function spaces in the (fixed) reference domains $\widehat{\Omega}$, $\widehat{\Omega}_f$, $\widehat{\Omega}_s$, we define spaces for spatial discretization only. Rather than employing Bochner-spaces [14, 61] for space-time functions, the time t is later explicitly accounted for, e.g., [21] (Section 7.1). Here, let $I := [0, T]$ be the time interval and T the end time value. First we define

$$\widehat{V} := H^1(\widehat{\Omega})^d.$$

Next, in the fluid domain, we define further:

$$\begin{aligned} \widehat{L}_f &:= L^2(\widehat{\Omega}_f), \\ \widehat{L}_f^0 &:= L^2(\widehat{\Omega}_f)/\mathbb{R}, \\ \widehat{V}_f^0 &:= \{\widehat{v}_f \in H^1(\widehat{\Omega}_f)^d : \widehat{v}_f = 0 \text{ on } \widehat{\Gamma}_{\text{in}} \cup \widehat{\Gamma}_D\}, \\ \widehat{V}_{f, \widehat{u}}^0 &:= \{\widehat{u}_f \in H^1(\widehat{\Omega}_f)^d : \widehat{u}_f = \widehat{u}_s \text{ on } \widehat{\Gamma}_i, \widehat{u}_f = 0 \text{ on } \widehat{\Gamma}_{\text{in}} \cup \widehat{\Gamma}_D \cup \widehat{\Gamma}_{\text{out}}\}, \\ \widehat{V}_{f, \widehat{u}, \widehat{\Gamma}_i}^0 &:= \{\widehat{\psi}_f \in H^1(\widehat{\Omega}_f)^d : \widehat{\psi}_f = 0 \text{ on } \widehat{\Gamma}_i \cup \widehat{\Gamma}_{\text{in}} \cup \widehat{\Gamma}_D \cup \widehat{\Gamma}_{\text{out}}\}. \end{aligned}$$

In the solid domain, we use

$$\begin{aligned} \widehat{L}_s &:= L^2(\widehat{\Omega}_s)^d, \\ \widehat{V}_s^0 &:= \{\widehat{u}_s \in H^1(\widehat{\Omega}_s)^d : \widehat{u}_s = 0 \text{ on } \widehat{\Gamma}_D\}. \end{aligned}$$

For the FSI problem using variational-monolithic coupling [40, 19, 20] the velocity spaces are extended from $\widehat{\Omega}_f$ and $\widehat{\Omega}_s$ to the entire domain $\widehat{\Omega}$ such that we can work with global H^1 functions. Thus, we define:

$$\widehat{V}^0 := \{\widehat{v} \in H^1(\widehat{\Omega})^d : \widehat{v} = 0 \text{ on } \widehat{\Gamma}_{\text{in}} \cup \widehat{\Gamma}_D\}. \quad (1)$$

By this choice, the kinematic and dynamic coupling conditions are automatically satisfied in a variational sense.

Finally, we notice that the spaces on the current domains $\Omega, \Omega_f, \Omega_s$ are defined correspondingly without ‘hat’ notation.

2.3 The ALE concept, transformed fluid flow, and solids in Lagrangian coordinates

In this section, we recapitulate the ingredients to formulate a coupled problem (i.e., fluid-structure interaction) with the help of the ALE approach. The ALE mapping $\widehat{\mathcal{A}} : \widehat{\Omega}_f \rightarrow \Omega_f$ is defined first.

2.3.1 The ALE transformation and ALE time-derivative

First, we define the ALE transformation:

Definition 2.1. *The ALE mapping is defined in terms of the vector-valued (artificial) fluid mesh displacement $\widehat{u}_f : \widehat{\Omega}_f \rightarrow \mathbb{R}^d$ such that*

$$\widehat{\mathcal{A}}(\widehat{x}, t) : \widehat{\Omega}_f \times I \rightarrow \Omega_f, \quad \text{with } \widehat{\mathcal{A}}(\widehat{x}, t) = \widehat{x} + \widehat{u}_f(\widehat{x}, t), \quad (2)$$

which is specified through the deformation gradient and its determinant

$$\widehat{F} := \widehat{\nabla} \widehat{\mathcal{A}} = \widehat{I} + \widehat{\nabla} \widehat{u}_f, \quad \widehat{J} := \det(\widehat{F}). \quad (3)$$

Furthermore, function values in Eulerian and Lagrangian coordinates are identified by

$$u_f(x) =: \widehat{u}_f(\widehat{x}), \quad \text{with } x = \widehat{\mathcal{A}}(\widehat{x}, t). \quad (4)$$

Here, \widehat{I} denotes the identity matrix. The mesh velocity is defined by $\widehat{w} := \partial_t \widehat{\mathcal{A}}$. The key quantity to measure the fluid mesh regularity is \widehat{J} . The artificial fluid displacement \widehat{u}_f (the mesh motion) is obtained in this work by solving a biharmonic equation [35, 58, 19, 57].

Finally, the transformation between different coordinate systems requires transformation of derivatives. For a vector-valued function $u \in \Omega$ and $\widehat{u} \in \widehat{\Omega}$ it holds, e.g., [39]:

$$\nabla u = \widehat{\nabla} \widehat{u} \widehat{F}^{-1}.$$

Finally, the ALE time-derivative is the total derivative of an Eulerian field and is important when working on moving domains:

$$\partial_t|_{\widehat{\mathcal{A}}} v_f(x, t) = \widehat{w} \cdot \nabla v_f + \partial_t v_f(x, t). \quad (5)$$

2.4 Equations for fluids and solids

In this section, we briefly state the basic underlying equations first separately. In the following, we first present fluid flow and then the solid part.

2.4.1 Strong forms

The isothermal, incompressible Navier-Stokes equations in an ALE setting read: Given v_{in} , h_f , and v_0 ; find $v_f : \Omega_f(t) \times I \rightarrow \mathbb{R}^d$ and $p_f : \Omega_f(t) \times I \rightarrow \mathbb{R}$ such that

$$\begin{aligned} \rho_f \partial_t|_{\hat{\mathcal{A}}} v_f + \rho_f (v_f - \hat{w}) \cdot \nabla v_f - \nabla \cdot \sigma_f(v_f, p_f) &= 0, & \nabla \cdot v_f &= 0 \quad \text{in } \Omega_f(t), \\ v_f^D &= v_{\text{in}} \text{ on } \Gamma_{\text{in}}, & v_f &= 0 \text{ on } \Gamma_D, & -p_f n_f + \rho_f \nu_f \nabla v_f \cdot n_f &= 0 \text{ on } \Gamma_{\text{out}}, & v_f &= h_f \text{ on } \Gamma_i, \\ v_f(0) &= v_0 \text{ in } \Omega_f(0), \end{aligned}$$

where the (symmetric) Cauchy stress is given by

$$\sigma_f(v_f, p_f) := -pI + \rho_f \nu_f (\nabla v + \nabla v^T),$$

with the density ρ_f and the kinematic viscosity ν_f . Later in the FSI problem, the function h_f will be given by the solid velocity v_s . The normal vector is denoted by n_f .

The equations for geometrically non-linear elastodynamics are given as follows: Given \hat{h}_s , \hat{u}_0 , and \hat{v}_0 ; find $\hat{u}_s : \hat{\Omega}_s \times I \rightarrow \mathbb{R}^d$ such that

$$\begin{aligned} \hat{\rho}_s \partial_t^2 \hat{u}_s - \hat{\nabla} \cdot (\hat{F} \hat{\Sigma}) &= 0 \quad \text{in } \hat{\Omega}_s, \\ \hat{u}_s &= 0 \text{ on } \hat{\Gamma}_D, & \hat{F} \hat{\Sigma} \cdot \hat{n}_s &= \hat{h}_s \text{ on } \hat{\Gamma}_i, \\ \hat{u}_s(0) &= \hat{u}_0 \text{ in } \hat{\Omega}_s \times \{0\}, & \hat{v}_s(0) &= \hat{v}_0 \text{ in } \hat{\Omega}_s \times \{0\}. \end{aligned}$$

The constitutive law is given by the tensor:

$$\hat{\Sigma} = \hat{\Sigma}_s(\hat{u}_s) = 2\mu \hat{E} + \lambda \text{tr}(\hat{E})I, \quad \text{with } \hat{E} = \frac{1}{2}(\hat{F}^T \hat{F} - I). \quad (6)$$

Here, μ and λ are the Lamé coefficients for the solid. The solid density is denoted by $\hat{\rho}_s$ and the solid deformation gradient is $\hat{F} = \hat{I} + \hat{\nabla} \hat{u}_s$. Later in FSI, the vector-valued function \hat{h}_s will be given by the normal stress from the fluid problem. Furthermore, \hat{n}_s denotes the normal vector.

2.4.2 Variational forms

The previous Navier-Stokes equations in a variational ALE framework described in a reference domain $\hat{\Omega}_f$ are given by:

Formulation 2.2 (ALE Navier-Stokes in $\hat{\Omega}_f$). *Let \hat{v}_f^D a suitable extension of Dirichlet inflow data. Find vector-valued velocities and a scalar-valued pressure $\{\hat{v}_f, \hat{p}_f\} \in \{\hat{v}_f^D + \hat{V}_f^0\} \times \hat{L}_f^0$ such that the initial data $\hat{v}_f(0) = \hat{v}_f^0$ are satisfied, and for almost all times $t \in I$ holds:*

$$\begin{aligned} \hat{\rho}_f (\hat{J} \partial_t \hat{v}_f, \hat{\psi}_f^v)_{\hat{\Omega}_f} + \hat{\rho}_f (\hat{J} \hat{F}^{-1} (\hat{v}_f - \hat{w}) \cdot \hat{\nabla} \hat{v}_f, \hat{\psi}_f^v)_{\hat{\Omega}_f} + (\hat{J} \hat{\sigma}_f \hat{F}^{-T}, \hat{\nabla} \hat{\psi}_f^v)_{\hat{\Omega}_f} \\ - \langle \hat{J} \hat{g}_f \hat{F}^{-T} \hat{n}_f, \hat{\psi}_f^v \rangle_{\hat{\Gamma}_{\text{out}}} - \langle \hat{J} \hat{\sigma}_f \hat{F}^{-T} \hat{n}_f, \hat{\psi}_f^v \rangle_{\hat{\Gamma}_i} = 0 \quad \forall \hat{\psi}_f^v \in \hat{V}_f^0, \\ (\widehat{\text{div}} (\hat{J} \hat{F}^{-1} \hat{v}_f), \hat{\psi}_f^p)_{\hat{\Omega}_f} = 0 \quad \forall \hat{\psi}_f^p \in \hat{L}_f^0. \end{aligned}$$

Here, $\hat{g}_f := -\hat{\rho}_f \nu_f \hat{F}^{-T} \hat{\nabla} \hat{v}_f^T$ denotes a correction term on the outflow boundary and \hat{n}_f is the outer normal vector. The transformed Cauchy stress tensor reads:

$$\hat{\sigma}_f = -\hat{p}_f \hat{I} + 2\hat{\rho}_f \nu_f (\hat{\nabla} \hat{v}_f \hat{F}^{-1} + \hat{F}^{-T} \hat{\nabla} \hat{v}_f^T). \quad (7)$$

The variational formulation for elastodynamics can be formulated as a first-order-in-time system:

Formulation 2.3 (First order system in time weak formulation of elasticity including strong damping). Find $\widehat{u}_s \in \widehat{V}_s^0$ and $\widehat{v}_s \in \widehat{L}_s$ with the initial data $\widehat{u}_s(0) = \widehat{u}_0$ and $\widehat{v}_s(0) = \widehat{v}_0$ such that for almost all times $t \in I$:

$$\begin{aligned} \widehat{\rho}_s(\partial_t \widehat{v}_s, \widehat{\psi}_s^v)_{\widehat{\Omega}_s} + (\widehat{F}\widehat{\Sigma}, \widehat{\nabla}\widehat{\psi}_s^v)_{\widehat{\Omega}_s} - \langle \widehat{F}\widehat{\Sigma}\widehat{n}_s, \widehat{\psi}_s^v \rangle_{\widehat{\Gamma}_i} &= 0 \quad \forall \widehat{\psi}_s^v \in \widehat{V}_s^0, \\ \widehat{\rho}_s(\partial_t \widehat{u}_s - \widehat{v}_s, \widehat{\psi}_s^u)_{\widehat{\Omega}_s} &= 0 \quad \forall \widehat{\psi}_s^u \in \widehat{L}_s. \end{aligned}$$

2.5 Variational-monolithic ALE fluid-structure interaction

2.5.1 FSI interface coupling conditions

The coupling of a fluid with a solid must satisfy two physical conditions; namely continuity of velocities and continuity of normal stresses. A third condition of geometric nature is necessary when working with the ALE framework: continuity of displacements, which couples the physical solid \widehat{u}_s and the fluid mesh motion \widehat{u}_f . Mathematically, the first and third conditions can be classified as (non-homogeneous) Dirichlet conditions and the second condition is a (non-homogeneous) Neumann condition.

In variational-monolithic coupling these Dirichlet conditions are built into the corresponding function space by employing a globalized Sobolev space \widehat{V}^0 (see (1)). Neumann type conditions are weakly incorporated through interface integrals, which actually cancel out in the later models because of their weak continuity thanks to working with the space \widehat{V}^0 .

For the fluid problem, continuity of velocities is required (i.e., a kinematic coupling condition):

$$\widehat{v}_f = \widehat{v}_s \quad \text{on } \widehat{\Gamma}_i. \quad (8)$$

To complete the solid problem, we must enforce the balance of the normal stresses on the interface (i.e., a dynamic coupling condition):

$$\widehat{J}\widehat{\sigma}_f\widehat{F}^{-T}\widehat{n}_f + \widehat{F}\widehat{\Sigma}\widehat{n}_s = 0 \quad \text{on } \widehat{\Gamma}_i. \quad (9)$$

For the geometric problem we have

$$\widehat{u}_f = \widehat{u}_s \quad \text{on } \widehat{\Gamma}_i, \quad (10)$$

from which we obtain immediately $\partial_t \widehat{u}_s = \widehat{v}_s = \widehat{v}_f$ on $\widehat{\Gamma}_i$ by temporal differentiation.

2.5.2 The FSI model using biharmonic mesh motion

Combining the previous equations for fluids and solids and applying biharmonic mesh motion for realizing the ALE mapping, we obtain the following FSI model [19, 57, 58]:

Formulation 2.4 (Variational-monolithic ALE FSI in $\widehat{\Omega}$). Let the constitutive laws from before be given and $\widehat{\alpha} > 0$ be a small parameter. Find a global vector-valued velocity, vector-valued displacements, additional displacements (due to the splitting of the biharmonic mesh motion model into two second-order equations) and a scalar-valued fluid pressure, i.e., $\{\widehat{v}, \widehat{u}_f, \widehat{u}_s, \widehat{w}, \widehat{p}_f\} \in \{\widehat{v}^D + \widehat{V}^0\} \times \{\widehat{u}_f^D + \widehat{V}_{f,\widehat{u}}^0\} \times$

$\{\widehat{u}_s^D + \widehat{V}_s^0\} \times \widehat{V} \times \widehat{L}_f^0$, such that $\widehat{v}(0) = \widehat{v}^0$, $\widehat{u}_f(0) = \widehat{u}_f^0$, and $\widehat{u}_s(0) = \widehat{u}_s^0$ are satisfied, and for almost all times $t \in I$ holds:

$$\begin{aligned}
& \text{Fluid/solid momentum} \left\{ \begin{aligned} & (\widehat{J}\widehat{\rho}_f\partial_t\widehat{v}, \widehat{\psi}^v)_{\widehat{\Omega}_f} + (\widehat{\rho}_f\widehat{J}(\widehat{F}^{-1}(\widehat{v} - \widehat{w}) \cdot \widehat{\nabla})\widehat{v}), \widehat{\psi}^v)_{\widehat{\Omega}_f} + (\widehat{J}\widehat{\sigma}_f\widehat{F}^{-T}, \widehat{\nabla}\widehat{\psi}^v)_{\widehat{\Omega}_f} \\ & + \langle \widehat{\rho}_f\nu_f\widehat{J}(\widehat{F}^{-T}\widehat{\nabla}\widehat{v}^T\widehat{n}_f)\widehat{F}^{-T}, \widehat{\psi}^v \rangle_{\widehat{\Gamma}_{out}} \\ & + (\widehat{\rho}_s\partial_t\widehat{v}, \widehat{\psi}^v)_{\widehat{\Omega}_s} + (\widehat{F}\widehat{\Sigma}, \widehat{\nabla}\widehat{\psi}^v)_{\widehat{\Omega}_s} = 0 \quad \forall \widehat{\psi}^v \in \widehat{V}^0, \end{aligned} \right. \\
& \text{Fluid mesh motion (biharmonic/split)} \left\{ \begin{aligned} & (\widehat{\alpha}\widehat{\nabla}\widehat{w}|_{\widehat{\Omega}_f}, \widehat{\nabla}\widehat{\psi}^u)_{\widehat{\Omega}_f} = 0 \quad \forall \widehat{\psi}_f^u \in \widehat{V}_{f,\widehat{u},\widehat{\Gamma}_i}^0, \\ & (\widehat{\alpha}\widehat{w}, \widehat{\psi}^w)_{\widehat{\Omega}} - (\widehat{\alpha}\widehat{\nabla}\widehat{u}_{f,s}, \widehat{\nabla}\widehat{\psi}^w)_{\widehat{\Omega}} = 0 \quad \forall \widehat{\psi}^w \in \widehat{V} \end{aligned} \right. \\
& \text{Solid momentum, 2nd eq.} \left\{ \widehat{\rho}_s(\partial_t\widehat{u}_s - \widehat{v})|_{\widehat{\Omega}_s}, \widehat{\psi}_s^u)_{\widehat{\Omega}_s} = 0 \quad \forall \widehat{\psi}_s^u \in \widehat{L}_s, \right. \\
& \text{Fluid mass conservation} \left\{ (\widehat{\text{div}}(\widehat{J}\widehat{F}^{-1}\widehat{v}), \widehat{\psi}_f^p)_{\widehat{\Omega}_f} = 0 \quad \forall \widehat{\psi}_f^p \in \widehat{L}_f^0. \right.
\end{aligned}$$

The Neumann coupling conditions on $\widehat{\Gamma}_i$ are fulfilled in a variational way and cancel in monolithic modeling due to the global test space \widehat{V}^0 in which the test functions from both the fluid and the solid subdomains coincide on the interface. Thus, the condition

$$\langle \widehat{J}\widehat{\sigma}_f\widehat{F}^{-T}\widehat{n}_f, \widehat{\psi}^v \rangle_{\widehat{\Gamma}_i} + \langle \widehat{F}\widehat{\Sigma}\widehat{n}_s, \widehat{\psi}^v \rangle_{\widehat{\Gamma}_i} = 0 \quad \forall \widehat{\psi}^v \in \widehat{V}^0 \quad (11)$$

is implicitly contained in the above system.

3 Discretization

In this section, we discuss temporal and spatial discretization of the forward problem. Our derivation contains many details on all terms of the FSI forward problem. The overall problem can be posed, however, in an abstract fashion, which facilitates the derivation of the backward-in-time adjoint problem in Section 4.

3.1 Temporal discretization

Our goal is to apply A-stable finite differences in time. Specifically, time discretization is based on a One-step- θ scheme as presented for the pure FSI problem, Formulation 2.4, in [58].

In more detail, semi-discretization in time yields a sequence of generalized steady-state problems that are completed by appropriate boundary values at every time step. Let

$$I = \{0\} \cup I_1 \cup \dots \cup I_N$$

be a partition of the time interval I into half open subintervals $I_n := (t_{n-1}, t_n]$ of (time step) size $k := k_n := t_n - t_{n-1}$ with

$$0 = t_0 < \dots < t_N = T.$$

Time derivatives are discretized with a backward difference quotient such that

$$\partial_t\widehat{u} \approx \frac{\widehat{u} - \widehat{u}^{n-1}}{k}, \quad \partial_t\widehat{v} \approx \frac{\widehat{v} - \widehat{v}^{n-1}}{k},$$

where $\hat{u} := \hat{u}^n := \hat{u}(t_n)$, $\hat{v} := \hat{v}^n := \hat{v}(t_n)$, $\hat{u}^{n-1} := \hat{u}(t_{n-1})$, $\hat{v}^{n-1} := \hat{v}(t_{n-1})$. Furthermore, the mesh velocity $\partial_t \hat{\mathcal{A}} = \hat{w}$ is numerically realized as $\hat{w} = k^{-1}(\hat{u}_f - \hat{u}_f^{n-1})$.

Formulation 3.1 (The time-discretized abstract problem). *We aim to find $\hat{U}^n = \{\hat{v}^n, \hat{u}_f^n, \hat{u}_s^n, \hat{w}^n, \hat{p}_f^n\} \in \hat{X}_D^0$, where $\hat{X}_D^0 := \{\hat{v}^D + \hat{V}^0\} \times \{\hat{u}_f^D + \hat{V}_{f,\hat{u}}^0\} \times \hat{V}_s^0 \times \hat{V} \times \hat{L}_f^0$ and $\hat{X} = \hat{V}^0 \times \hat{V}_{f,\hat{u},\hat{\Gamma}_i}^0 \times \hat{V}_s^0 \times \hat{V} \times \hat{L}_f^0$, for all $n = 1, 2, \dots, N$ such that*

$$\hat{A}(\hat{U}^n)(\hat{\Psi}) = 0 \quad \forall \hat{\Psi} \in \hat{X}, \quad (12)$$

where the semi-linear form $\hat{A}(\cdot)(\cdot)$ is split into

$$\hat{A}(\hat{U}^n)(\hat{\Psi}) := \hat{A}_T(\hat{U}^n)(\hat{\Psi}) + \hat{A}_I(\hat{U}^n)(\hat{\Psi}) + \hat{A}_E(\hat{U}^n)(\hat{\Psi}) + \hat{A}_P(\hat{U}^n)(\hat{\Psi}).$$

Details of this decomposition are provided in Definition 3.2.

Definition 3.2 (Arranging the semi-linear form $\hat{A}(\hat{U}^n)(\hat{\Psi})$ into groups). *We formally split the semi-linear form into four categories: time equation terms (including the time derivatives); implicit terms (such as the fluid incompressibility and also the biharmonic mesh motion); pressure terms; and finally all ‘standard’ terms (e.g., stress terms, fluid convection). We then obtain the decomposition:*

$$\begin{aligned} \hat{A}_T(\hat{U})(\hat{\Psi}) &= (\hat{J}\hat{\rho}_f\partial_t\hat{v}, \hat{\psi}^v)_{\hat{\Omega}_f} - (\hat{\rho}_f\hat{J}(\hat{F}^{-1}\hat{w} \cdot \hat{\nabla})\hat{v}, \hat{\psi}^v)_{\hat{\Omega}_f} + (\hat{\rho}_s\partial_t\hat{v}, \hat{\psi}^v)_{\hat{\Omega}_s} + (\hat{\rho}_s\partial_t\hat{u}_s, \hat{\psi}_s^u)_{\hat{\Omega}_s}, \\ \hat{A}_I(\hat{U})(\hat{\Psi}) &= (\hat{\alpha}\hat{\nabla}\hat{w}|_{\hat{\Omega}_f}, \hat{\nabla}\hat{\psi}^u)_{\hat{\Omega}_f} + (\hat{\alpha}\hat{w}, \hat{\psi}^w)_{\hat{\Omega}} - (\hat{\alpha}\hat{\nabla}\hat{u}_{f,s}, \hat{\nabla}\hat{\psi}^w)_{\hat{\Omega}} + (\text{div}(\hat{J}\hat{F}^{-1}\hat{v}), \hat{\psi}_f^p)_{\hat{\Omega}_f}, \\ \hat{A}_P(\hat{U})(\hat{\Psi}) &= (\hat{J}\hat{\sigma}_{f,p}\hat{F}^{-T}, \hat{\nabla}\hat{\psi}^v)_{\hat{\Omega}_f}, \\ \hat{A}_E(\hat{U})(\hat{\Psi}) &= (\hat{\rho}_f\hat{J}(\hat{F}^{-1}\hat{v} \cdot \hat{\nabla})\hat{v}, \hat{\psi}^v)_{\hat{\Omega}_f} + (\hat{J}\hat{\sigma}_{f,vu}\hat{F}^{-T}, \hat{\nabla}\hat{\psi}^v)_{\hat{\Omega}_f} \\ &\quad + \langle \rho_f\nu\hat{J}(\hat{F}^{-T}\hat{\nabla}v_f^T)\hat{F}^{-T}\hat{n}, \hat{\psi}^v \rangle_{\hat{\Gamma}_{out}} + (\hat{F}\hat{\Sigma}, \hat{\nabla}\hat{\psi}^v)_{\hat{\Omega}_s} - (\hat{\rho}_s\hat{v}, \hat{\psi}_s^u)_{\hat{\Omega}_s}, \end{aligned} \quad (13)$$

where the fluid stress tensor $\hat{\sigma}_f$ is further split into $\hat{\sigma}_{f,vu}$, $\hat{\sigma}_{f,p}$:

$$\hat{\sigma}_{f,p} = -\hat{p}_f\hat{I}, \quad \hat{\sigma}_{f,vu} = \rho_f\nu_f(\hat{\nabla}\hat{v}\hat{F}^{-1} + \hat{F}^{-T}\hat{\nabla}\hat{v}^T).$$

The (nonlinear) time derivative in $\hat{A}_T(\hat{U})(\hat{\Psi})$ is approximated by a backward difference quotient. For the time step $t_n \in I$, for $n = 1, 2, \dots, N$ ($N \in \mathbb{N}$), we compute $\hat{v} := \hat{v}^n$, $\hat{u}_i := \hat{u}_i^n$ ($i = f, s$) via

$$\begin{aligned} \hat{A}_T(\hat{U}^n)(\hat{\Psi}) &\approx \frac{1}{k}(\hat{\rho}_f\hat{J}^{n,\theta}(\hat{v} - \hat{v}^{n-1}), \hat{\psi}^v)_{\hat{\Omega}_f} - \frac{1}{k}(\hat{\rho}_f(\hat{J}\hat{F}^{-1}(\hat{u}_f - \hat{u}_f^{n-1}) \cdot \hat{\nabla})\hat{v}, \hat{\psi}^v)_{\hat{\Omega}_f} \\ &\quad + \frac{1}{k}(\hat{\rho}_s(\hat{v} - \hat{v}^{n-1}), \hat{\psi}^v)_{\hat{\Omega}_s} + \frac{1}{k}(\hat{\rho}_s(\hat{u}_s - \hat{u}_s^{n-1}), \hat{\psi}_s^u)_{\hat{\Omega}_s} \\ &=: \frac{1}{k}\hat{A}_{T,k}(\hat{U}^n, \hat{U}^{n-1,t}, \hat{\Psi}), \end{aligned}$$

where we introduce the parameter $\theta \in [0, 1]$. Furthermore, we use

$$\hat{J}^{n,\theta} = \theta\hat{J}^n + (1 - \theta)\hat{J}^{n-1},$$

and $\hat{u}_i^n := \hat{u}_i(t_n)$, $\hat{v}^n := \hat{v}(t_n)$, and $\hat{J} := \hat{J}^n := \hat{J}(t_n)$. In our computations in Section 6, we always consider $\hat{J}^{n,0.5}$. The former time step is given by \hat{v}^{n-1} , etc. for $i = f, s$.

Formulation 3.3. Let the previous time step solution $\widehat{U}^{n-1} = \{\widehat{v}^{n-1}, \widehat{u}_f^{n-1}, \widehat{u}_s^{n-1}, \widehat{w}^{n-1}, \widehat{p}_f^{n-1}\}$ and the time step $k := k_n = t_n - t_{n-1}$ be given. In order to solve (12), we seek $\widehat{U}^n = \{\widehat{v}^n, \widehat{u}_f^n, \widehat{u}_s^n, \widehat{w}^n, \widehat{p}_f^n\} \in \widehat{X}^0$ by employing one-step- θ splitting:

$$\widehat{A}_{T,k}(\widehat{U}^n, \widehat{U}^{n-1})(\widehat{\Psi}) + \theta k \widehat{A}_E(\widehat{U}^n)(\widehat{\Psi}) + k \widehat{A}_P(\widehat{U}^n)(\widehat{\Psi}) + k \widehat{A}_I(\widehat{U}^n)(\widehat{\Psi}) = -(1-\theta)k \widehat{A}_E(\widehat{U}^{n-1})(\widehat{\Psi}). \quad (14)$$

The concrete scheme depends on the choice of the parameter $\theta \in [0, 1]$. For $\theta = 1$ we obtain the strongly A-stable backward Euler scheme (BE). If $k < 0.5$, for $\theta = 0.5 + k$, we obtain the 2nd order (shown for linear parabolic problems in [50, 36]), A-stable, globally stabilized, Crank-Nicolson scheme (CNs).

Remark 3.4. Formulation 3.3 is still nonlinear and continuous on the spatial level.

3.2 Spatial discretization

The time discretized formulation is the starting point for the Galerkin discretization in space. To this end, we construct a finite dimensional subspace $\widehat{X}_h^0 \subset \widehat{X}^0$ to find an approximate solution to the continuous problem. As previously explained, in the context of our variational-monolithic formulation, the computations are done on the reference configuration $\widehat{\Omega}$. We use two dimensional shape-regular meshes. A mesh consists of quadrilateral cells \widehat{K} . They perform a non-overlapping cover of the computation domain $\widehat{\Omega} \subset \mathbb{R}^d$, $d = 2$. The corresponding mesh is given by $\widehat{\mathcal{T}}_h = \{\widehat{K}\}$. The discretization parameter in the reference configuration is denoted by \widehat{h} and is a cell-wise constant that is given by the diameter $\widehat{h}_{\widehat{K}}$ of the cell \widehat{K} .

On $\widehat{\mathcal{T}}_h$, the conforming finite element space for $\{\widehat{v}_h, \widehat{u}_{f,h}, \widehat{u}_{s,h}, \widehat{p}_{f,h}, \widehat{w}_h\}$ is denoted by the space $\widehat{X}_h \subset \widehat{X}$. For Navier-Stokes flow, i.e., $\{\widehat{v}_h, \widehat{p}_{f,h}\}$, we prefer the biquadratic, discontinuous-linear Q_2^c/P_1^{dc} element. For the specific definitions of the single elements, we refer the reader to [13]. The property of the Q_2^c/P_1^{dc} element is continuity of the velocity values across different mesh cells [31]. However, the pressure is defined by discontinuous test functions. Therefore, this element preserves local mass conservation, is of low order, gains the *inf-sup stability*, and is an optimal choice for both fluid problems and fluid-structure interaction problems. The two displacement variables, namely $\widehat{u}_h, \widehat{w}_h$ are discretized with Q_2^c elements.

In total, the discretized forward problem consists of

Formulation 3.5. Given $\widehat{U}^0 \in \widehat{X}$ finding $\widehat{U} = (\widehat{U}_h^n)_{n=1}^N \in \widehat{X}_h^N$ solving

$$\sum_{n=1}^N \left(\widehat{A}_{T,k}(\widehat{U}_h^n, \widehat{U}_h^{n-1})(\widehat{\Psi}_h^n) + \theta k \widehat{A}_E(\widehat{U}_h^n)(\widehat{\Psi}_h^n) + k \widehat{A}_P(\widehat{U}_h^n)(\widehat{\Psi}_h^n) + k \widehat{A}_I(\widehat{U}_h^n)(\widehat{\Psi}_h^n) + (1-\theta)k \widehat{A}_E(\widehat{U}_h^{n-1})(\widehat{\Psi}_h^n) \right) = 0 \quad \forall (\widehat{\Psi}_h^n)_{n=1}^N \in \widehat{X}_h^N. \quad (15)$$

This abstract formulation serves as basis to derive the adjoint state in Section 4.

4 Gradient computation

We are interested in identifying material parameters, e.g., μ in (6). To this end, we denote by $q \in \mathbb{R}^p$, with $p \geq 1$, the collection of these parameters, and will define suitable cost functionals $\mathcal{J}(q, \widehat{U})$ to be minimized. To highlight the dependence of the equation on the parameters q , we add an additional q argument to the form \widehat{A}_E , e.g., we consider $\widehat{A}_E(q, \widehat{U}_h^n)(\widehat{\Psi}_h^n)$ instead of $\widehat{A}_E(\widehat{U}_h^n)(\widehat{\Psi}_h^n)$ in (15).

Assuming that (15) admits a unique solution for any given q , we can obtain an optimality system by the standard Lagrange formalism, see, e.g., [46, 55, 38]. For a rigorous proof of the required differentiability properties, some progress has been made for stationary FSI-problems in [60]. A rigorous derivation of the corresponding adjoints in the context of shape optimization can be found in [34].

The formal Lagrange approach provides an adjoint equation to (15) as

Formulation 4.1. Find $\widehat{Z} \in \widehat{X}_h^N$ solving

$$\begin{aligned} \sum_{n=1}^N \left(\partial_{\widehat{U}_h^n} \widehat{A}_{T,k}(\widehat{U}_h^n, \widehat{U}_h^{n-1})(\widehat{\Psi}_h^n, \widehat{Z}_h^n) + \partial_{\widehat{U}_h^{n-1}} \widehat{A}_{T,k}(\widehat{U}_h^n, \widehat{U}_h^{n-1})(\widehat{\Psi}_h^{n-1}, \widehat{Z}_h^n) \right. \\ \left. + \theta k \partial_{\widehat{U}_h^n} \widehat{A}_E(q, \widehat{U}_h^n)(\widehat{\Psi}_h^n, \widehat{Z}_h^n) + k \partial_{\widehat{U}_h^n} \widehat{A}_P(\widehat{U}_h^n)(\widehat{\Psi}_h^n, \widehat{Z}_h^n) + k \partial_{\widehat{U}_h^n} \widehat{A}_I(\widehat{U}_h^n)(\widehat{\Psi}_h^n, \widehat{Z}_h^n) \right. \\ \left. + (1 - \theta)k \partial_{\widehat{U}_h^{n-1}} \widehat{A}_E(q, \widehat{U}_h^{n-1})(\widehat{\Psi}_h^{n-1}, \widehat{Z}_h^n) \right) = \partial_{\widehat{U}} \mathcal{J}(q, \widehat{U})(\widehat{\Psi}) \quad \forall (\widehat{\Psi}_h^n)_{n=1}^N \in \widehat{X}_h^N. \end{aligned} \quad (16)$$

Here $\partial_{\widehat{U}_h^n} \widehat{A}$ denotes the directional derivative of the form \widehat{A} with respect to its \widehat{U}_h^n argument, and the first argument of the second parentheses denotes the respective direction.

With this adjoint, we obtain the total derivative of the cost functional $q \mapsto \mathcal{J}(q) := \mathcal{J}(q, \widehat{U})$ in a direction δq as

$$\frac{d}{dq} \mathcal{J}(q, \widehat{U}) \delta q = \partial_q \mathcal{J}(q, \widehat{U})(\delta q) + \sum_{n=1}^N \left(\theta k \partial_q \widehat{A}_E(q, \widehat{U}_h^n)(\delta q, \widehat{Z}_h^n) + (1 - \theta)k \partial_q \widehat{A}_E(q, \widehat{U}_h^{n-1})(\delta q, \widehat{Z}_h^n) \right)$$

allowing the calculation of the reduced gradient $\nabla J(q) \in \mathbb{R}^p$ of the cost functional by

$$(\nabla J(q), \delta q) = \frac{d}{dq} \mathcal{J}(q, \widehat{U}) \delta q \quad \forall \delta q \in \mathbb{R}^p \quad (17)$$

cf., e.g., [5].

5 Solution algorithms

In order to minimize the cost functional $\mathcal{J}(q)$, we employ a standard globalized gradient method, i.e.,

Algorithm 1 (Gradient method). Let $q^0 \in \mathbb{R}^p$ be an initial guess, and pick parameters $\gamma \in (0, 1/2)$ and $\beta \in (0, 1)$. For $k = 0, 1, \dots$ until $\|\nabla_q \mathcal{J}(q^k)\|_Q < TOL$ iterate

1. Solve the (nonlinear) primal problem (15) to obtain $\widehat{U}_h \in \widehat{X}_h^N$ using Algorithm 2.
2. Solve the (linear) adjoint problem (16) to obtain $\widehat{Z}_h \in \widehat{X}_h^N$.

3. Compute the gradient $\nabla\mathcal{J}(q^k)$ using (17).
4. Find the largest $l \in \{0, 1, \dots\}$ such that (Armijo-rule)

$$\mathcal{J}(q^k - \beta^l \nabla\mathcal{J}(q^k)) \leq \mathcal{J}(q^k) - \gamma\beta^l \|\nabla\mathcal{J}(q^k)\|^2$$

holds and set $\beta_k = \beta^l$.

5. Update

$$q^{k+1} = q^k - \beta_k \nabla\mathcal{J}(q^k).$$

In the first step of the previous algorithm for solving the nonlinear primal problem, we employ the following Newton method. At each time point the following problem is given:

$$\widehat{A}(\widehat{U}_h^n)(\widehat{\Psi}) = 0 \quad \forall \widehat{\Psi} \in \widehat{X}_h.$$

Algorithm 2 (Residual-based Newton's method). We omit h and n for the convenience of the reader. Choose an initial Newton guess $\widehat{U}^0 \in \widehat{X}$. For the iteration steps $k = 0, 1, 2, 3, \dots$:

1. Find $\delta\widehat{U}^k \in \widehat{X}^0$ such that

$$\widehat{A}'(\widehat{U}^k)(\delta\widehat{U}^k, \widehat{\Psi}) = -\widehat{A}(\widehat{U}^k)(\widehat{\Psi}) \quad \forall \widehat{\Psi} \in \widehat{X}, \quad (18)$$

$$\widehat{U}^{k+1} = \widehat{U}^k + \lambda_k \delta\widehat{U}^k, \quad (19)$$

for $\lambda_k = 1$. The arising linear equations are solved with a direct method; namely UMFPAK [15]. This choice is justified since the spatial numbers of degrees of freedom is moderate in our numerical examples. Moreover, in order to save computational cost, we adopt simplified Newton steps; i.e., the matrix $\widehat{A}'(\widehat{U}^k)(\delta\widehat{U}^k, \widehat{\Psi})$ is only rebuild when $\lambda_k^l < 1$ (defined below) or $\|\widehat{A}(\widehat{U}^k)\| \in [0.001, 1]\|\widehat{A}(\widehat{U}^{k-1})\|$.

2. The criterion for convergence is the contraction of the residuals:

$$\|\widehat{A}(\widehat{U}^{k+1})\| < \|\widehat{A}(\widehat{U}^k)\|. \quad (20)$$

3. If (20) is violated, re-compute in (19) \widehat{U}^{k+1} by choosing $\lambda_k = 0.6^l$, and compute for $l = 1, \dots, l_M$ (e.g. $l_M = 5$) a new solution

$$\widehat{U}^{k+1} = \widehat{U}^k + \lambda_k^l \delta\widehat{U}^k$$

until (20) is fulfilled for a $l^* < l_M$ or l_M is reached. In the latter case, no convergence is obtained and the program aborts.

4. In case of $l^* < l_M$ we check next the (relative) stopping criterion:

$$\|\widehat{A}(\widehat{U}^{k+1})\| \leq \|\widehat{A}(\widehat{U}^0)\| \text{TOL}_N.$$

If this is criterion is fulfilled, set $\widehat{U}^n := \widehat{U}^{k+1}$. Otherwise, we increment $k \rightarrow k + 1$ and goto Step 1.

6 Numerical tests

We conduct several numerical tests in this section. These are implemented in the open-source package DOpElib [18, 32] using the finite elements of deal.II [1].

An open-source implementation of (15), used as basis for our computations, can be found in DOpElib [18, 32] in `Examples/PDE/InstatPDE/Example2`.

6.1 Material parameters

The material parameters for the FSI-1 and FSI-3 tests are chosen as proposed in [41, 9] and listed in Table 1. The parameters for the flapping example are a mixture of [30, 59, 24].

	FSI-1	FSI-3	Flapping
ν_f	$10^{-3} \frac{\text{m}^2}{\text{s}}$	$10^{-3} \frac{\text{m}^2}{\text{s}}$	$10^{-1} \frac{\text{cm}^2}{\text{s}}$
μ_s	$0.5 \cdot 10^6 \frac{\text{kg}}{\text{m s}^2}$	$2.0 \cdot 10^6 \frac{\text{kg}}{\text{m s}^2}$	$1.0 \cdot 10^9 \frac{\text{g}}{\text{cm s}^2}$
ν_s	0.4	0.4	0.4
$\hat{\rho}_s$	$10^3 \frac{\text{kg}}{\text{m}^3}$	$10^3 \frac{\text{kg}}{\text{m}^3}$	$10^2 \frac{\text{g}}{\text{cm}^3}$
$\hat{\rho}_f$	$10^3 \frac{\text{kg}}{\text{m}^3}$	$10^3 \frac{\text{kg}}{\text{m}^3}$	$10^2 \frac{\text{g}}{\text{cm}^3}$

Table 1: Material parameters for all test cases.

6.2 Example 1: Parameter estimation within the FSI 1 benchmark

In this first numerical example, we consider a quasi-stationary setting based on the FSI 1 benchmark [41, 9]. The optimization problem reads: identify the Lamé parameter μ_s from measurements of the beam-tip displacement at $A := (0.6, 0.2)$. The exact values u_d are taken from a reference solution with $\mu = 0.5 \cdot 10^6 \frac{\text{kg}}{\text{m s}^2}$.

The forward problem is solved with the backward Euler scheme, i.e., $\theta = 1$, since the configuration is stationary and we only use a time-dependent method to find the stationary limit.

6.2.1 Cost functional

The cost functional reads:

$$J(q, \hat{U}) = \frac{1}{2} (\hat{u}_1(A, T) - u_d)^2 + \frac{\alpha}{2} |q - q_d|^2,$$

with $q_d = 2.27007 \cdot 10^{-5}$.

6.2.2 Configuration

The geometry of the FSI-1 and FSI-3 settings are displayed in Figure 1. An elastic beam is attached to a cylinder and is surrounded by an incompressible fluid. The initial geometry is once uniformly

refined in space.

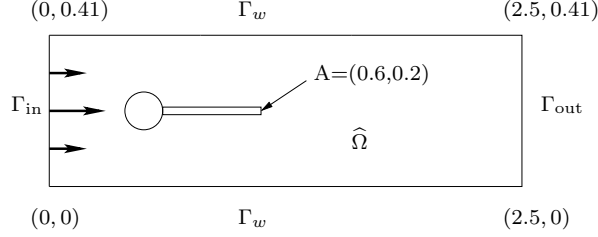


Figure 1: FSI-1 and FSI-3 benchmarks (Examples 1 and 2): flow around cylinder with elastic beam with circle-center $C = (0.2, 0.2)$ and radius $r = 0.05$.

On the cylinder and outer boundary Γ_w we enforce zero Dirichlet boundary conditions for \hat{v} and \hat{u} . On the outflow boundary Γ_{out} we prescribe the do-nothing outflow condition [37]. The inflow profile on Γ_{in} is given by:

$$\hat{v}(0, y) := 1.5 y (0.41 - y) \frac{4}{0.41^2} v_{\text{mean}}(t).$$

The mean inflow $v_{\text{mean}}(t)$ is 0.2 m/s for Example 1 (FSI 1) and 2.0 m/s in Example 2 (FSI 3). In the FSI 1 test case, we compute $n = 25$ time steps using $k = 1$ s and in the FSI 3 example, we work with $k = 0.001$ s with $T = 0.6$ s corresponding to $n = 6000$ time steps.

6.2.3 Discussion of the FSI 1 findings

Our results for three different configurations are displayed in the Tables 2, 3, and 4. In the first run with $\alpha = 0.001$, the algorithm converges slowly in order to estimate q^k and to reduce the cost functional $\mathcal{J}(q^k)$. The main reason is due to the low regularization, which is confirmed by two further runs with $\alpha = 0.1$ and 1.

In Table 3, the value of α is enlarged to 0.1. Here, in 155 gradient iterations, the cost functional is reduced by a order to 10^{14} from an initial control $q^0 = 5000$ to $q^{155} = 10^6$.

Increasing further α to 1 (Table 3) yields a reduction in $\mathcal{J}(q^k)$ from about 10^{11} to 10^{-6} . The gradient algorithm converges in 5 iterations.

6.3 Example 2: Optimal control within the FSI 3 benchmark

In this second numerical test, we employ the same geometry as in Example 1. The material parameters and boundary data can be found in Table 1 and Section 6.2.2. We now consider an optimal control problem in which μ_s is detected in such a way to match the displacement value at the beam tip at $(0.6, 0.4)$ obtained by the FSI 1 simulation in Example 1. Since this numerical test is nonstationary with periodic solutions in the original forward run, we use the shifted Crank-Nicolson time-stepping scheme with minimal numerical dissipation.

6.3.1 Cost functional

The cost functional is given by:

$$J(q, \hat{U}) = \frac{1}{2} (\hat{u}_1(A, T) - u_d)^2 + \frac{\alpha}{2} |q - q_d|^2$$

Table 2: Optimization results for the FSI 1 example with $\alpha = 0.001$ and $q_d = \cdot 10^6$. The initial Residual in $q_0 = 5\,000$ is $|\nabla \mathcal{J}(q^0)| = 987.5$

Iter	$\mathcal{J}(q^k)$	q^k	$\frac{ \nabla \mathcal{J}(q^k) }{ \nabla \mathcal{J}(q^0) }$
0	$4.913 \cdot 10^8$	5000	$1.0000 \cdot 10^{-0}$
1	$4.9033 \cdot 10^8$	5987.54	$9.9901 \cdot 10^{-1}$
2	$4.8936 \cdot 10^8$	6974.11	$9.9802 \cdot 10^{-1}$
3	$4.8838 \cdot 10^8$	7959.69	$9.9703 \cdot 10^{-1}$
\vdots	\vdots	\vdots	\vdots
101	$4.0201 \cdot 10^8$	99950.5	$9.0457 \cdot 10^{-1}$
102	$4.0121 \cdot 10^8$	100844	$9.0367 \cdot 10^{-1}$
103	$4.0042 \cdot 10^8$	101736	$9.0278 \cdot 10^{-1}$
\vdots	\vdots	\vdots	\vdots
198	$3.3157 \cdot 10^8$	182600	$8.2151 \cdot 10^{-1}$
199	$3.3091 \cdot 10^8$	183411	$8.2069 \cdot 10^{-1}$
200	$3.3025 \cdot 10^8$	184222	$8.1988 \cdot 10^{-1}$
\vdots	\vdots	\vdots	\vdots

Table 3: Optimization results for the FSI 1 example with $\alpha = 0.1$ and $q_d = 10^6$. The initial Residual in $q_0 = 5\,000$ is $|\nabla \mathcal{J}(q^0)| = 9.875 \cdot 10^4$

Iter	$\mathcal{J}(q^k)$	q^k	$\frac{ \nabla \mathcal{J}(q^k) }{ \nabla \mathcal{J}(q^0) }$
0	$4.913 \cdot 10^{10}$	5000	$1.0000 \cdot 10^{-0}$
1	$3.9862 \cdot 10^{10}$	103754	$9.0075 \cdot 10^{-1}$
2	$3.2342 \cdot 10^{10}$	192707	$8.1135 \cdot 10^{-1}$
3	$2.6241 \cdot 10^{10}$	272832	$7.3082 \cdot 10^{-1}$
\vdots	\vdots	\vdots	\vdots
101	$3.3216 \cdot 10^1$	999974	$2.6001 \cdot 10^{-5}$
102	$2.6950 \cdot 10^1$	999977	$2.3421 \cdot 10^{-5}$
103	$2.1865 \cdot 10^1$	999979	$2.1096 \cdot 10^{-5}$
\vdots	\vdots	\vdots	\vdots
154	$5.1211 \cdot 10^{-4}$	10^6	$1.0210 \cdot 10^{-7}$
155	$4.1550 \cdot 10^{-4}$	10^6	$9.1962 \cdot 10^{-8}$

with $q_d = 2.27007 \cdot 10^{-5}$, i.e., the functional is similar to Example 1 and the reference value comes from FSI 1, but not FSI 3.

6.3.2 Discussion of the FSI 3 findings

Graphical plots of the solution are provided in Figure 2. Our quantitative results are shown in Table 5. The gradient algorithm converges in 29 iterations in which the cost functional is reduced by 10^3 and

Table 4: Optimization results for the FSI 1 example with $\alpha = 1$ and $q_d = 500\,000$. The initial Residual in $q_0 = 5\,000$ is $|\nabla\mathcal{J}(q^0)| = 4.913 \cdot 10^5$

Iter	$\mathcal{J}(q^k)$	q^k	$\frac{ \nabla\mathcal{J}(q^k) }{ \nabla\mathcal{J}(q^0) }$
0	$1.216 \cdot 10^{11}$	5000	$1.0000 \cdot 10^{-0}$
1	$6.8268 \cdot 10^6$	496291	$7.4929 \cdot 10^{-3}$
2	$3.8328 \cdot 10^2$	499972	$5.6144 \cdot 10^{-5}$
3	$2.1519 \cdot 10^{-2}$	500000	$4.2068 \cdot 10^{-7}$
4	$1.2082 \cdot 10^{-6}$	500000	$3.1522 \cdot 10^{-9}$

the control is approximated by $q^{29} = 572\,378$.

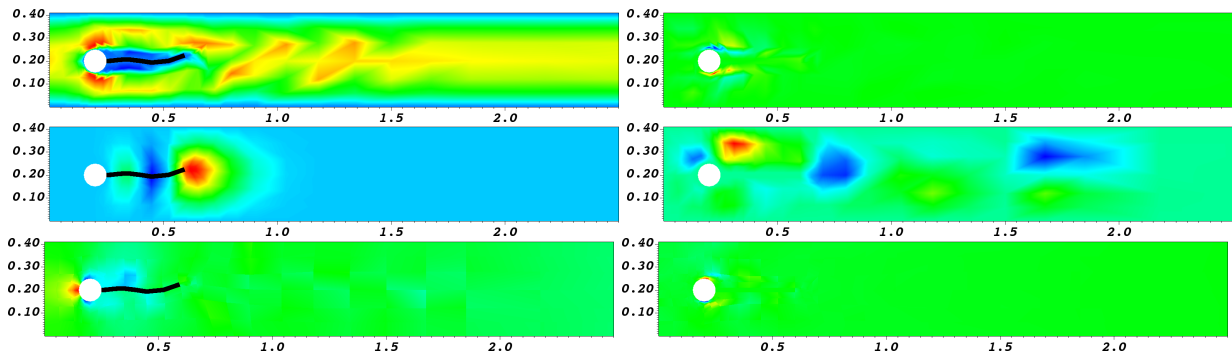


Figure 2: Example 2: At $T = 5s$ (time step No. 5000): $v_x(t), u_y(t)$ and $p(t)$ in the deformed configuration $\Omega(t)$. Left column: the primal states are shown. Right column: the corresponding adjoint states are shown.

Table 5: Optimization results for the FSI-3 example with $\alpha = 0.1$ and $q_d = 500\,000$. The initial Residual in $q_0 = 2 \cdot 10^6$ is $1.489 \cdot 10^5$

Iter	$\mathcal{J}(q^k)$	q^k	$\frac{ \nabla\mathcal{J}(q^k) }{ \nabla\mathcal{J}(q^0) }$
0	$1.117 \cdot 10^{11}$	$2 \cdot 10^6$	$1.0000 \cdot 10^{-0}$
1	$9.0593 \cdot 10^{10}$	$1.85112 \cdot 10^6$	$9.0075 \cdot 10^{-1}$
2	$7.3502 \cdot 10^{10}$	$1.71702 \cdot 10^6$	$8.1135 \cdot 10^{-1}$
3	$5.9636 \cdot 10^{10}$	$1.59623 \cdot 10^6$	$7.3082 \cdot 10^{-1}$
4	$4.8386 \cdot 10^{10}$	$1.48743 \cdot 10^6$	$6.5829 \cdot 10^{-1}$
\vdots	\vdots	\vdots	\vdots
28	$3.2041 \cdot 10^8$	580353	$5.3569 \cdot 10^{-2}$
29	$2.5996 \cdot 10^8$	572378	$4.8252 \cdot 10^{-2}$

6.4 Example 3: Two-dimensional flapping membranes

In this third example, we consider two-dimensional flap dynamics. This test is a challenge because of the thin flaps and the mesh regularity. The original setups for forward simulations were inspired

by [30]. Our configuration here is a further extension, towards FSI-optimization, of [59] and [24].

6.4.1 Cost functional

The cost functional is given by:

$$J(q, \hat{U}) = F(\hat{\Gamma}_{\text{opt}}, T) + \frac{\alpha}{2} |q - q_d|^2$$

where T is the end time value as in the other examples and $F(\cdot)$ is the drag functional defined as

$$F(\hat{\Gamma}_{\text{opt}}, T) := \int_{\hat{\Gamma}_{\text{opt}}} (\hat{\sigma}_f \cdot \hat{n}) \cdot e_1 \, ds$$

where \hat{n} is the unit normal vector pointing outward of the domain $\hat{\Omega}_s$ and e_1 the first unit vector in \mathbb{R}^2 . The boundary part, where the drag is evaluated is

$$\hat{\Gamma}_{\text{opt}} := \{2 \leq x \leq 8; y = 0\}.$$

Moreover, we notice that we only control μ in the valves, while in the rest of the solid, the value is as in Table 1.

6.4.2 Configuration

The geometry is shown in Figure 3. The initial mesh is once uniformly refined yielding the mesh shown in Figure 4.

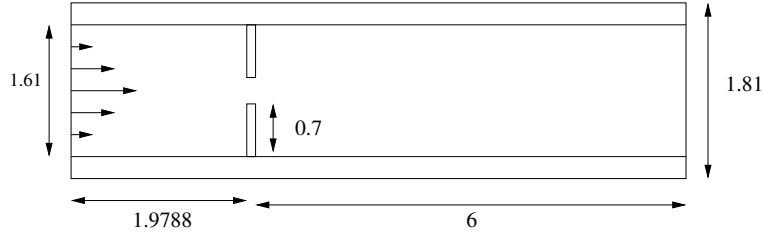


Figure 3: Example 3: Configuration. All data given in cm.

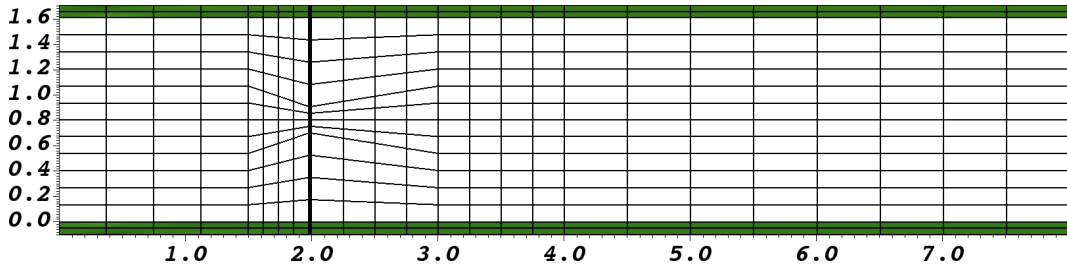


Figure 4: The mesh for the flapping membranes example at the initial time step. All geometric values are given in cm. The solid boundaries are colored in dark green. The flaps are located at $1.9788 \text{ cm} \leq x \leq 2.0 \text{ cm}$.

On the inflow boundary, $\widehat{\Gamma}_{\text{in}} := \{x = 0; -0.1 \leq y \leq 1.61\}$, we prescribe a parabolic inflow profile

$$v(0, y) := 0.15y(1.61 - y) \frac{4}{1.61^2} v_{\text{mean}}(t) \quad \text{for } t \in I := [0, 0.9],$$

where $v_{\text{mean}}(t)$ taken from Figure 5.

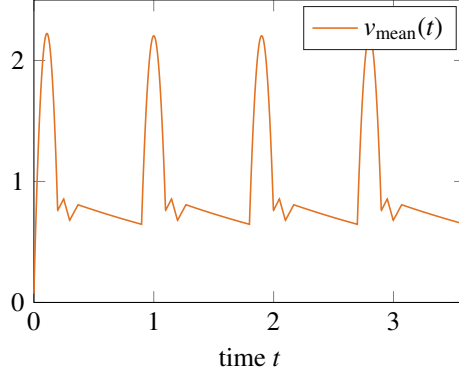


Figure 5: Interpolated flow rate profile $\bar{v}(t)$ that is used to scale the inflow profile of the flapping membrane example.

At the outflow boundary the do-nothing outflow condition $\widehat{\Gamma}_{\text{out}}$ is prescribed for \widehat{v} and \widehat{p} , while the displacements are fixed there. On the outer wall boundaries

$$\widehat{\Gamma}_{\text{wall}} := \{0 \leq x \leq 8; y = -0.1\} \cup \{0 \leq x \leq 8; y = -1.61\}$$

we use homogeneous Neumann conditions for the displacements and the velocity in order to allow the solid to move freely.

The computations are performed on the time interval $I = (0, 0.579375 \text{ s})$. The end time value $T = 0.579375 \text{ s}$ is chosen such that the first maximal stress appears for the initial control q^0 . For the computations, the time interval is split into 618 time steps.

6.4.3 Discussion of the flapping membrane findings

The flow and pressure fields in the physical configuration $\Omega(t)$ are displayed in Figure 6. Therein, it is visible that the solid flaps undergo large deformations. In the optimized configuration after 8 cycles the flaps even deform more. Here, a robust mesh motion model is indispensable. In Table 6, the performance of the optimization procedure is shown. A reduction of 10^{12} in the cost functional is achieved. The optimal q^8 is $5 \cdot 10^6$.

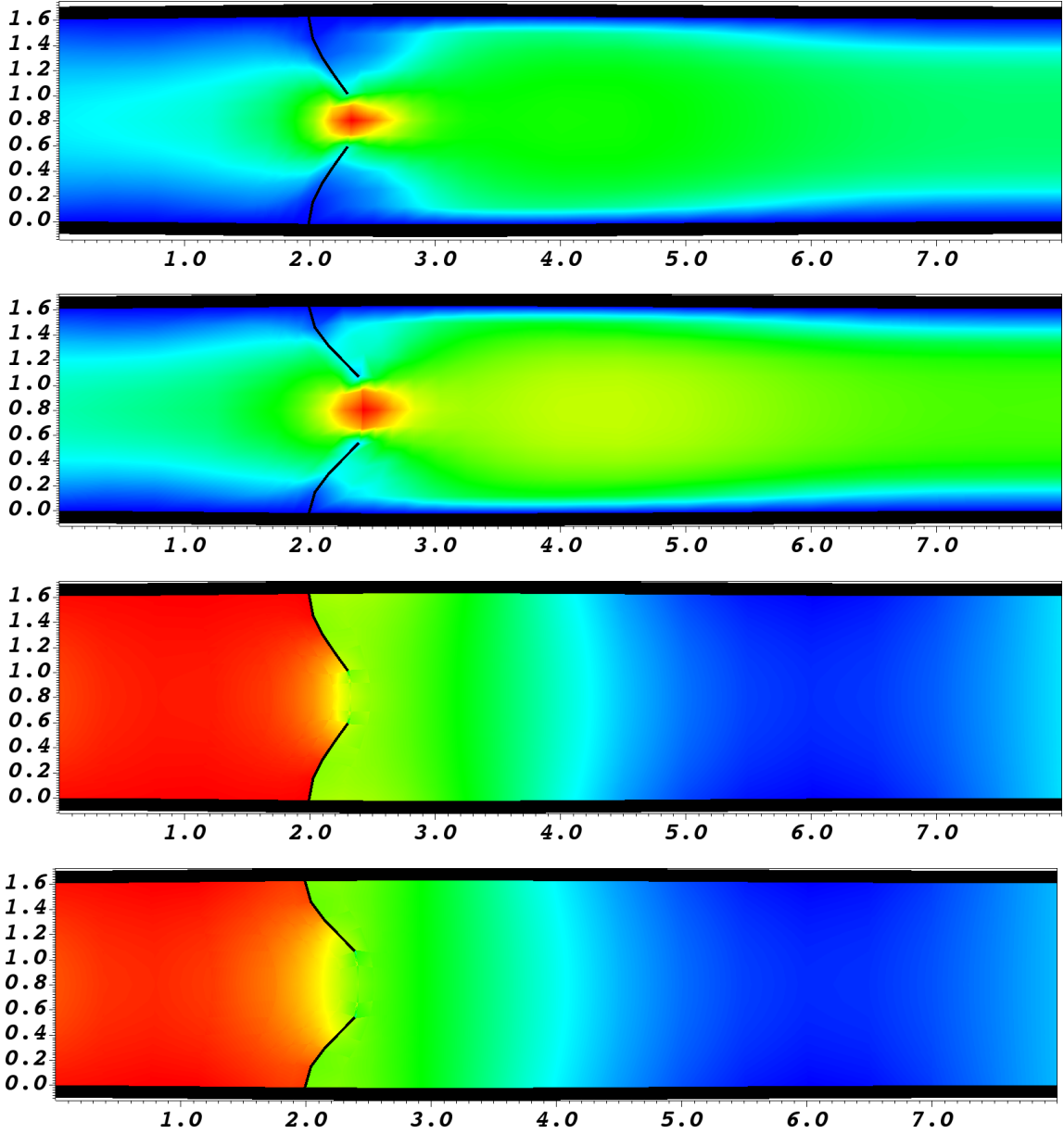


Figure 6: Example 3: At $T = 0.579375$ s (time step No. 618): $v_x(t)$ and $p(t)$ are displayed in the deformed configuration $\Omega(t)$. Going from top to bottom: $v_x(t = 0.579375$ s) in the optimization cycle 0 (classical forward run with $\mu = q^0 = 2 \cdot 10^7$). The maximum velocity (in red) has the value 3.15 cm/s. In the 2nd row, $v_x(t = 0.579375$ s) in the eighth optimization cycle is displayed; here $\mu = q^8 = 5 \cdot 10^6$, which means less-stiff flaps and corresponding higher displacements. Consequently, the maximum velocity is reduced and has the value 2.3 cm/s. In the rows three and four the corresponding pressure fields are shown. The maximum pressure values are $3012 \frac{\text{g}}{\text{cm s}^2}$ and $2825 \frac{\text{g}}{\text{cm s}^2}$, respectively.

Table 6: Optimization results for the flapping membrane example with $\alpha = 1$ and $q_d = 5 \cdot 10^6$. The initial Residual in $q_0 = 2 \cdot 10^7$ is $|\nabla \mathcal{J}(q^0)| = 1.686 \cdot 10^7$

Iter	$\mathcal{J}(q^k)$	q^k	$\frac{ \nabla \mathcal{J}(q^k) }{ \nabla \mathcal{J}(q^0) }$
0	$1.265 \cdot 10^{14}$	$2 \cdot 10^7$	$1.0000 \cdot 10^{-0}$
1	$1.9517 \cdot 10^{12}$	$3.13665 \cdot 10^6$	$1.2422 \cdot 10^{-1}$
2	$3.0118 \cdot 10^{10}$	$5.23147 \cdot 10^6$	$1.5432 \cdot 10^{-2}$
3	$4.6476 \cdot 10^8$	$4.97125 \cdot 10^6$	$1.9170 \cdot 10^{-3}$
4	$7.1728 \cdot 10^6$	$5.00357 \cdot 10^6$	$2.3813 \cdot 10^{-4}$
5	$1.1151 \cdot 10^5$	$4.99956 \cdot 10^6$	$2.9582 \cdot 10^{-5}$
6	$2.5424 \cdot 10^3$	$5.00006 \cdot 10^6$	$3.6747 \cdot 10^{-6}$
7	$8.6090 \cdot 10^2$	$4.99999 \cdot 10^6$	$4.5649 \cdot 10^{-7}$
8	$8.3495 \cdot 10^2$	$5 \cdot 10^6$	$5.6707 \cdot 10^{-8}$

7 Conclusions

In this work, we developed settings for FSI-based optimization. Therein, the FSI problem is nonlinear and nonstationary and allows for large solid deformations. Consequently, when working with the ALE technique, a robust mesh motion model must be chosen. In this work, it is based on a biharmonic equation. Based on this forward model, we provide the adjoint state, which is running backward-in-time. The resulting FSI-optimization problem is solved with a gradient-type method. Three numerical examples are designed to investigate the performance of our algorithmic techniques. In the first numerical test an extension of the steady-state FSI 1 benchmark is considered. In the second and third examples, fully nonstationary tests are investigated. Specifically, the last numerical test is numerically challenging, even for the forward problem, because the flaps are very thin, while undergoing large solid deformations. Here, we observe significant reductions of the cost functional and excellent convergence properties of the optimization algorithm.

References

- [1] G. Alzetta, D. Arndt, W. Bangerth, V. Boddu, B. Brands, D. Davydov, R. Gassmoeller, T. Heister, L. Heltai, K. Kormann, M. Kronbichler, M. Maier, J.-P. Pelteret, B. Turcksin, and D. Wells. The `deal.II` library, version 9.0. *J. Numer. Math.*, 26(4):173–183, 2018.
- [2] M. Asterino, F. Chouly, and F. Fernández. An added-mass free semi-implicit coupling scheme for fluid-structure interaction. *C. R. Acad. Sci. Paris, Sér. I.*, 347(1-2):99–104, 2009.
- [3] Y. Bazilevs, M.-C. Hsu, and M. Bement. Adjoint-based control of fluid-structure interaction for computational steering applications. *Procedia Computer Science*, 18:1989–1998, 2013. 2013 International Conference on Computational Science.
- [4] Y. Bazilevs, K. Takizawa, and T. Tezduyar. *Computational Fluid-Structure Interaction: Methods and Applications*. Wiley, 2013.

- [5] R. Becker, D. Meidner, and B. Vexler. Efficient numerical solution of parabolic optimization problems by finite element methods. *Optim. Methods Softw.*, 22(5):813–833, 2007.
- [6] C. Bertoglio, P. Moireau, and J. Gerbeau. Sequential parameter estimation in fluid-structure problems. application to hemodynamics. *Int. J. Numer. Meth. Biomed. Engrg.*, 28:434–455, 2012.
- [7] T. Bodnár, G. Galdi, and Š. Nečasová. *Fluid-Structure Interaction and Biomedical Applications*. Advances in Mathematical Fluid Mechanics. Springer Basel, 2014.
- [8] F. Bucci and I. Lasiecka. Optimal boundary control with critical penalization for a pde model of fluid-solid interactions. *Calc. Var.*, 37(1-2):217–235, 2010.
- [9] H.-J. Bungartz, M. Mehl, and M. Schäfer. *Fluid-Structure Interaction II: Modelling, Simulation, Optimization*. Lecture Notes in Computational Science and Engineering. Springer, 2010.
- [10] H.-J. Bungartz and M. Schäfer. *Fluid-Structure Interaction: Modelling, Simulation, Optimization*, volume 53 of *Lecture Notes in Computational Science and Engineering*. Springer, 2006.
- [11] P. Causin, J.-F. Gerbeau, and F. Nobile. Added-mass effect in the design of partitioned algorithms for fluid-structure problems. *Comput. Methods Appl. Mech. Engrg.*, 194:4506–4527, 2005.
- [12] L. Chirco, R. D. Vià, and S. Manservigi. An optimal control method for fluid structure interaction systems via adjoint boundary pressure. *Journal of Physics: Conference Series*, 923:012026, 2017.
- [13] P. G. Ciarlet. *The finite element method for elliptic problems*. North-Holland, Amsterdam [u.a.], 2. pr. edition, 1987.
- [14] R. Dautray and J.-L. Lions. *Mathematical Analysis and Numerical Methods for Science and Technology*, volume 5. Springer-Verlag, Berlin-Heidelberg, 2000.
- [15] T. A. Davis and I. S. Duff. An unsymmetric-pattern multifrontal method for sparse LU factorization. *SIAM J. Matrix Anal. Appl.*, 18(1):140–158, 1997.
- [16] J. Degroote, M. Hojjat, E. Stavropoulou, R. Wüchner, and K.-U. Bletzinger. Partitioned solution of an unsteady adjoint for strongly coupled fluid-structure interactions and application to parameter identification of a one-dimensional problem. *Struct. Multidisc. Optim.*, 47(1):77–94, 2013.
- [17] J. Donéa, P. Fasoli-Stella, and S. Giuliani. Lagrangian and Eulerian finite element techniques for transient fluid-structure interaction problems. In *Trans. 4th Int. Conf. on Structural Mechanics in Reactor Technology*, page Paper B1/2, 1977.
- [18] The Differential Equation and Optimization Environment: DOPELIB. published online <http://www.dopelib.net>. <http://www.dopelib.net>.

- [19] T. Dunne. *Adaptive Finite Element Approximation of Fluid-Structure Interaction Based on Eulerian and Arbitrary Lagrangian-Eulerian Variational Formulations*. PhD thesis, University of Heidelberg, Im Neuenheimer Feld 293/294, 2007.
- [20] T. Dunne, T. Richter, and R. Rannacher. *Numerical simulation of fluid-structure interaction based on monolithic variational formulations*, pages 1–75. Contemporary Challenges in Mathematical Fluid Mechanics. Springer, World Scientific, Singapore, 2010.
- [21] L. C. Evans. *Partial differential equations*. American Mathematical Society, 2000.
- [22] L. Failer. *Optimal control of time-dependent nonlinear fluid-structure interaction*. PhD thesis, Technische Universität München, Boltzmannstr. 3, 2017.
- [23] L. Failer, D. Meidner, and B. Vexler. Optimal control of a linear unsteady fluid–structure interaction problem. *J. Optim. Theory Appl.*, 170(1):1–27, 2016.
- [24] L. Failer and T. Wick. Adaptive time-step control for nonlinear fluid-structure interaction. *Journal of Computational Physics*, 366:448–477, 2018.
- [25] L. Formaggia and F. Nobile. A stability analysis for the arbitrary Lagrangian Eulerian formulation with finite elements. *East-West Journal of Numerical Mathematics*, 7:105–132, 1999.
- [26] L. Formaggia, A. Quarteroni, and A. Veneziani. *Cardiovascular Mathematics: Modeling and simulation of the circulatory system*. Springer-Verlag, Italia, Milano, 2009.
- [27] C. Förster, W. A. Wall, and E. Ramm. Artificial added mass instabilities in sequential staggered coupling of nonlinear structures and incompressible viscous flows. *Computer Methods in Applied Mechanics and Engineering*, 196(7):1278–1293, 2007.
- [28] S. Frei, B. Holm, T. Richter, T. Wick, and H. Yang. *Fluid-structure interactions: Fluid-Structure Interaction: Modeling, Adaptive Discretisations and Solvers*. de Gruyter, 2017.
- [29] G. Galdi and R. Rannacher. *Fundamental Trends in Fluid-Structure Interaction*. World Scientific, 2010.
- [30] A. J. Gil, A. A. Carreno, J. Bonet, and O. Hassan. The immersed structural potential method for haemodynamic applications. *J. Comp. Physics*, 229:8613–8641, 2010.
- [31] V. Girault and P.-A. Raviart. *Finite Element method for the Navier-Stokes equations*. Number 5 in Computer Series in Computational Mathematics. Springer-Verlag, 1986.
- [32] C. Goll, T. Wick, and W. Wollner. DOPElib: Differential equations and optimization environment; A goal oriented software library for solving pdes and optimization problems with pdes. *Archive of Numerical Software*, 5(2):1–14, 2017.
- [33] T. Guerra, J. Tiago, and A. Sequeira. Optimal control in blood flow simulations. *International Journal of Non-Linear Mechanics*, 64:57–69, 2014.

- [34] J. Haubner, M. Ulbrich, and S. Ulbrich. Analysis of shape optimization problems for unsteady fluid-structure interaction. Technical report, Technische Universität München, Boltzmannstr. 3, 2019.
- [35] B. Helenbrook. Mesh deformation using the biharmonic operator. *Int. J. Numer. Methods Engrg.*, 56:1007–1021, 2003.
- [36] J. G. Heywood and R. Rannacher. Finite-element approximation of the nonstationary Navier-Stokes problem part iv: Error analysis for second-order time discretization. *SIAM Journal on Numerical Analysis*, 27(2):353–384, 1990.
- [37] J. G. Heywood, R. Rannacher, and S. Turek. Artificial boundaries and flux and pressure conditions for the incompressible Navier-Stokes equations. *International Journal of Numerical Methods in Fluids*, 22:325–352, 1996.
- [38] M. Hinze, R. Pinnau, M. Ulbrich, and S. Ulbrich. *Optimization with PDE Constraints*, volume 23 of *Mathematical Modelling: Theory and Applications*. Springer, 2009.
- [39] G. Holzapfel. *Nonlinear Solid Mechanics: A continuum approach for engineering*. John Wiley and Sons, LTD, 2000.
- [40] J. Hron and S. Turek. *A monolithic FEM/Multigrid solver for ALE formulation of fluid structure with application in biomechanics*, pages 146–170. Springer-Verlag, 2006.
- [41] J. Hron and S. Turek. *Proposal for numerical benchmarking of fluid-structure interaction between an elastic object and laminar incompressible flow*, volume 53, pages 146–170. Springer-Verlag, 2006.
- [42] T. Hughes, W. Liu, and T. Zimmermann. Lagrangian-Eulerian finite element formulation for incompressible viscous flows. *Comput. Methods Appl. Mech. Engrg.*, 29:329–349, 1981.
- [43] J. Kratzke. *Uncertainty Quantification for Fluid-Structure Interaction: Application to Aortic Biomechanics*. PhD thesis, University of Heidelberg, Im Neuenheimer Feld 293/294, 2018.
- [44] P. Kuberry and H. Lee. A decoupling algorithm for fluid-structure interaction problems based on optimization. *Computer Methods in Applied Mechanics and Engineering*, 267:594–605, 2013.
- [45] T. Lassila, A. Manzoni, A. Quarteroni, and G. Rozza. A reduced computational and geometrical framework for inverse problems in hemodynamics. *Int. J. Numer. Meth. Biomed. Engrg.*, 29(7):741–776, 2013.
- [46] J.-L. Lions. *Optimal Control of Systems Governed by Partial Differential Equations*. Die Grundlehren der mathematischen Wissenschaften. Springer, Berlin – Heidelberg – New York, 1. edition, 1971.
- [47] V. Martin, F. Clément, A. Decoene, and J.-F. Gerbeau. Parameter identification for a one-dimensional blood flow model. *ESAIM: Proc.*, 14:174–200, 2005.

- [48] M. Moubachir and J.-P. Zolésio. Optimal control of fluid-structure interaction systems : the case of a rigid solid. Research Report RR-4611, INRIA, 2002.
- [49] M. Perego, A. Veneziani, and C. Vergara. A variational approach for estimating the compliance of the cardiovascular tissue: An inverse fluid-structure interaction problem. *SIAM Journal on Scientific Computing*, 33(3):1181–1211, 2011.
- [50] R. Rannacher. On the stabilization of the Crank-Nicolson scheme for long time calculations. Preprint, August 1986.
- [51] T. Richter. Goal-oriented error estimation for fluidstructure interaction problems. *Computer Methods in Applied Mechanics and Engineering*, 223-224:28–42, 2012.
- [52] T. Richter. *Fluid-structure interactions: models, analysis, and finite elements*. Springer, 2017.
- [53] T. Richter and T. Wick. Optimal control and parameter estimation for stationary fluid-structure interaction. *SIAM J. Sci. Comput.*, 35(5):B1085–B1104, 2013.
- [54] K. Singhammer. *Optimal control of stationary fluid-structure interaction with partitioned methods*. PhD thesis, Technische Universität München, Boltzmannstr. 3, 2019.
- [55] F. Tröltzsch. *Optimal control of partial differential equations*, volume 112 of *Graduate Studies in Mathematics*. American Mathematical Society, Providence, RI, 2010.
- [56] van Brummelen E. H. Added mass effects of compressible and incompressible flows in fluid-structure interaction. *ASME. J. Appl. Mech.*, 76(2):021206, 2009.
- [57] T. Wick. *Adaptive Finite Element Simulation of Fluid-Structure Interaction with Application to Heart-Valve Dynamics*. PhD thesis, University of Heidelberg, Im Neuenheimer Feld 293/294, 2011.
- [58] T. Wick. Fluid-structure interactions using different mesh motion techniques. *Computers and Structures*, 89(13-14):1456–1467, 2011.
- [59] T. Wick. Flapping and contact FSI computations with the fluid-solid interface-tracking/interface-capturing technique and mesh adaptivity. *Computational Mechanics*, 53(1):29–43, 2014.
- [60] T. Wick and W. Wollner. On the differentiability of fluid–structure interaction problems with respect to the problem data. *J. Math. Fluid Mech.*, 21(3), 2019.
- [61] J. Wloka. *Partielle Differentialgleichungen*. B. G. Teubner Verlag, Stuttgart, 1982.
- [62] K. Zee, E. Brummelen, I. Akkerman, and R. Borst. Goal-oriented error estimation and adaptivity for fluid-structure interaction using exact linearized adjoints. *Computer Methods in Applied Mechanics and Engineering*, 200:2738–2757, 2011.